CSIRO PUBLISHING
Exploration Geophysics, 2015, **46**, 371–380
http://dx.doi.org/10.1071/EG14116

Direct simulation Monte Carlo method with a focal mechanism algorithm

Asep Nur Rachman[1] Tae Woong Chung[1,4] Kazuo Yoshimoto[2] Sukyoung Yun[3]

[1]Department of Energy and Mineral Resources Engineering, Sejong University, Seoul 143-747, Korea.
[2]Graduate School of Nanobioscience, Department of Materials System Science, Yokohama City University, Yokohama 236-0027, Japan.
[3]Korea Polar Research Institute, Incheon 406-840, Korea.
[4]Corresponding author. Email: chungtw@sejong.ac.kr

Abstract. To simulate the observation of the radiation pattern of an earthquake, the direct simulation Monte Carlo (DSMC) method is modified by implanting a focal mechanism algorithm. We compare the results of the modified DSMC method (DSMC-2) with those of the original DSMC method (DSMC-1). DSMC-2 shows more or similarly reliable results compared to those of DSMC-1, for events with 12 or more recorded stations, by weighting twice for hypocentral distance of less than 80 km. Not only the number of stations, but also other factors such as rough topography, magnitude of event, and the analysis method influence the reliability of DSMC-2. The most reliable result by DSMC-2 is obtained by the best azimuthal coverage by the largest number of stations. The DSMC-2 method requires shorter time steps and a larger number of particles than those of DSMC-1 to capture a sufficient number of arrived particles in the small-sized receiver.

Key words: direct simulation Monte Carlo (DSMC) method, focal mechanism, number of stations, receiver problem, seismic wave attenuation.

Received 18 November 2014, accepted 19 November 2014, published online 15 January 2015

Originally submitted to KSEG 30 September 2014, accepted 15 November 2014

Introduction

Seismic wave attenuation, usually expressed as Q^{-1}, is an indispensable parameter in understanding the interior state and tectonic history of the earth. In particular, regional information on Q^{-1} of high-frequency waves in the lithosphere is very helpful, not only for scientific research, but also for the practical purpose of simulating earthquake ground motion in engineering seismology (Yoshimoto et al., 1993). After the observation of lithospheric Q^{-1} at high frequency (Dainty, 1981), recent regional studies (e.g. Sato et al., 2012) have focused on the separation of the total seismic attenuation Q_t^{-1} (another form of Q^{-1}), into Q_i^{-1} and Q_s^{-1}, where Q_i^{-1} represents the intrinsic absorption caused by the conversion of elastic energy to heat, and Q_s^{-1} is the scattering attenuation caused by the redistribution of wave energy without any loss.

The most widely used approach to the separation into Q_i^{-1} and Q_s^{-1} is multiple lapse time window analysis (MLTWA), introduced almost simultaneously by Hoshiba et al. (1991) and Fehler et al. (1992). Based on the observations that the early portion of a seismogram is dominated by the direct S-wave whose amplitude is reduced by Q_t^{-1}, whereas the S-coda is composed entirely by scattered S-waves whose amplitude is reduced by Q_i^{-1} but enlarged by Q_s^{-1}, MLTWA simulates the integral of the observed energy from multiple earthquakes in three successive time windows.

The simulated values, based on radiative transfer theory, were first obtained analytically by Zeng et al. (1991) and Sato (1993) using a model with a uniformly distributed scatterer in a homogeneous half-space and a source located at the origin. The simulated values were also obtained by the Monte Carlo method, using an improved model with isotropic layers and variable source depth (Hoshiba, 1997). The simulation method was further improved by the direct simulation Monte Carlo (DSMC) method (Yoshimoto, 2000) using a velocity gradient in the layer model. The DSMC method, which utilises a finite difference scheme for ray tracing, is expected to be applicable to a three-dimensional structure model due to the simplicity of the algorithm.

Despite the improvement of the simulation method, the MLTWA method generally displays a large observational scatter in the first window. The main cause of this scatter is known to be the different radiation pattern of each earthquake (e.g. Fehler et al., 1992). The regional alteration of local structure has also been thought of as one of the causes of the observational scatter (e.g. Giampiccolo et al., 2006). In addition, the different focal depth of each earthquake may cause significant scatter, because large variations of Q^{-1} values of S-waves are well known in the crust and upper mantle (Mitchell and Xie, 1994; Mitchell, 1995). Recently, MLTWA, using single earthquake data, showed little observational scatter and presented reliable results despite the relative dearth of data (Asep et al., 2014).

To fit observation of the radiation pattern of an earthquake, the current study first attempts to implant a focal mechanism algorithm into the code of the DSMC method. As a comparison test, the same analysis is also performed using an unprocessed DSMC code. Hereafter, DSMC codes that are unprocessed and implanted with a focal mechanism are referred to as DSMC-1 and DSMC-2, respectively.

DSMC-1

The DSMC-1 method (Yoshimoto, 2000) synthesises the waves coda envelope in three-dimensional scattering media by using the number of energised particles moving out from a point source with a take-off angle (θ) and an azimuthal angle (φ) (Figure 1), which are mutually independent, random variables with values in the range of [0, π] and [0, 2π], respectively.

This method, however, assumes an isotropic source radiation and scattering of seismic waves with locally uniform coefficients of scattering $\eta_s\left(=\frac{2\pi f}{v}Q_s^{-1}\right)$ and intrinsic $\eta_i\left(=\frac{2\pi f}{v}Q_i^{-1}\right)$. Consider that the particle propagates over distance $v(z)\Delta t$, where $v(z)$ is the seismic velocity at depth z, and Δt is a short time interval. Then, the probability of a scattering event is represented by $\eta_s v(z)\Delta t$ (Feynman et al., 1989), and the occurrence of scattering in the distance $v(z)\Delta t$ is determined by the inequality:

$$\eta_s v(z)\Delta t > I, \tag{1}$$

where I is a random number between 0.0 and 1.0. If equation 1 is fulfilled, the particle moves to a different direction by the redetermination of θ and φ. In the x'–z plane (Figure 1), the particle location at time Δt follows the seismic ray theory expressed as the following:

$$(\Delta x', \Delta z) = [v(z)\Delta t \sin\vartheta, v(z)\Delta t \cos\vartheta], \tag{2}$$

where ϑ is the angle of particle propagation, initially $\vartheta = \theta$ at the source, and satisfies the following differential equation (Cervený and Ravindra, 1971):

$$\Delta\vartheta = \frac{dv(z)}{dz}\Delta t \sin\vartheta \tag{3}$$

The finite difference method at interval time $\Delta t = 0.2$ s was used for the propagation of the particles, whose number at source is 10^6 based on the Monte Carlo scheme.

Upon arrival in a receiver region with a volume element of ΔV, each particle was considered equivalent to a seismic energy packet. At the receiver, the energy of a particle at the source was reduced by exp $(-\eta_i\Delta t)$. Torus volume, just beneath the free surface, was assumed as a receiver (Figure 1) because the isotropic assumption of source radiation and scattering of seismic waves signify a spherical symmetry of the DSMC-1 method. The size of torus volume, with the thickness of 7 km and with the radius of epicentral distance, is large enough to stabilise the number of arrived particles but small enough to retain temporal resolution.

The DSMC-1 method showed better results than those of the analytical solution by using a depth-dependent velocity model (Chung et al., 2010) and a source with a depth of 10 km (Chung, 2014).

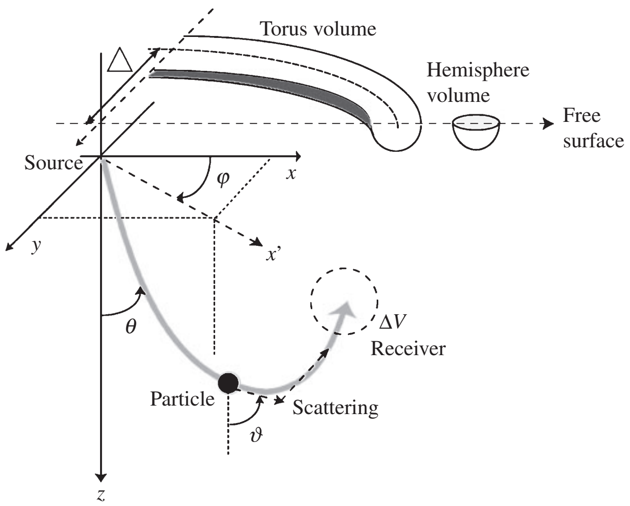

Fig. 1. Schematic diagram for an energised particle, starting from the source located at the origin of the Cartesian coordinate and drifting to a spherical-shaped receiver of volume ΔV, to count the number of the energised particles. Whereas the DSMC-1 used a torus-shaped receiver with the average radius proportional to the epicentral distance (△), DSMC-2 replaced the torus with a hemisphere. Both receivers are located just beneath the free surface.

DSMC-2

Based on the code of DSMC-1, the DSMC-2 method incorporated the radiation pattern of both traverse SV and SH waves by using well-known relations (Aki and Richards, 1980) as in equations 4 and 5:

$$\begin{aligned} \mathrm{SV}rad = {} & \sin\lambda\cos 2\delta\cos\theta\sin(\varphi-\phi_s) \\ & -\cos\lambda\cos\delta\cos 2\theta\cos(\varphi-\phi_s) \\ & +\frac{1}{2}\cos\lambda\sin\delta\sin 2\theta\sin 2(\varphi-\phi_s) \\ & -\frac{1}{2}\sin\lambda\sin 2\delta\sin 2\theta\sin 2(\varphi-\phi_s), \end{aligned} \tag{4}$$

$$\begin{aligned} \mathrm{SH}rad = {} & \cos\lambda\cos\delta\cos\theta\sin(\varphi-\phi_s) \\ & +\cos\lambda\sin\delta\sin\theta\cos 2(\varphi-\phi_s) \\ & +\sin\lambda\cos 2\delta\sin 2\theta\cos(\varphi-\phi_s) \\ & -\frac{1}{2}\sin\lambda\sin 2\delta\sin 2\theta\sin 2(\varphi-\phi_s) \end{aligned} \tag{5}$$

where ϕ_s, δ and λ represent the strike, dip and rake of the fault, respectively. This incorporation means an expanded application from the two-dimensional to the three-dimensional isotropic model, which was claimed as an advantage of the DSMC method over previous methods (Yoshimoto, 2000). The geometrical expansion, however, resulted in the torus volume being reduced to a small receiver with hemisphere volume (Figure 1), because a spherical symmetry of DSMC-1 was no longer available to DSMC-2.

In Figure 2, the amplitude of DSMC-2 is compared with DSMC-1 at a receiver with the hypocentral distance of 30 km. The azimuth of the receiver in DSMC-2 was 90° for the source at a

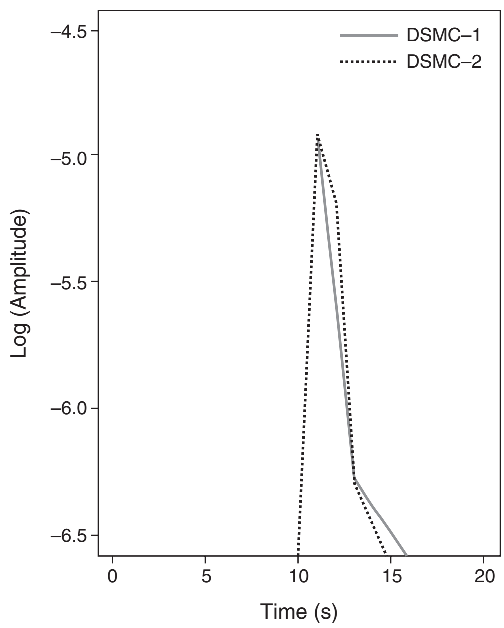

Fig. 2. Comparison of the amplitude between DSMC-1 (grey line) and DSMC-2 (black dotted lines) at a receiver with the hypocentral distance of 30 km. The azimuth of the receiver in DSMC-2 was 90° for the source at a depth of 10 km with focal mechanism parameters of strike = 180°, dip = 90°, and rake = 90°.

depth of 10 km with focal mechanism parameters of strike = 180°, dip = 90° and rake = 90°. By considering the small volume of the receiver in DSMC-2, we shoot 2×10^6 particles in DSMC-2, twice as many as those of DSMC-1, and shorten the interval time as $\Delta t = 0.1$ s. The envelopes of DSMC-2 are inflected around 12 s due to the anisotropic source radiation.

Data and processing

Our data are based on the study by Chung and Asep (2013), which used 41 events during the period of 1999 – 2009. Each event of depth and magnitude ranges from 6.1 to 16.9 km and from 2.0 to 4.8, respectively, which were recorded by 3 to 18 stations operated by the Korea Meteorological Agency (KMA) and the Korea Institute of Geoscience and Mineral Resources (KIGAM). From these events, DSMC-2 showed similar or smaller residuals – reliable results – than those of DSMC-1 for the events that have been recorded by 12 or more stations (see Tables 1 and 2). The results were obtained by MLTWA processing as follows. The MLTWA method was applied for each event with hypocentral distances less than 120 km. The first

Table 1. Earthquakes with more than 12 recorded stations. Focal mechanism parameters of events were obtained by Hong and Choi (2012), except event 5 (Park et al., 2007). In parameter evaluation, *P* denotes both the *P*-wave polarities and *S*/*P* amplitude ratios, and *I* denotes waveform inversion.

No	Date	Location			*M*	Num.	Focal mechanism			Method
	Y-M-D H:M:S	Lat.	Long.	Depth (km)		data	Strike	Dip	Rake	
1	2003–03–10 03 : 28 : 03	36.13	128.34	10.8	3.1	12	301	65	48	*P*
2	2004–01–04 21 : 11 : 52	36.15	127.03	9.6	2.9	12	297	57	–21	*P*
3	2004–04–26 04 : 29 : 26	35.83	128.23	10.5	3.9	13	139	71	47	*I*
4	2004–08–05 20 : 32 : 54	35.84	127.32	8.5	3.3	13	122	82	7	*I*
5	2004–09–27 09 : 47 : 34	35.48	128.28	16.9	2.5	16	97	85	–42	*P*
6	2007–01–20 11 : 56 : 53	37.68	128.59	10.0	4.8	13	203	86	–180	*I*
7	2009–05–01 22 : 58 : 28	36.55	128.71	13.3	4.0	18	307	73	41	*I*

Table 2. Comparison of M_{sum} between DSMC-1 and DSMC-2. The values in parentheses denote non-weighting values.

Event Number	DSMC-2	DSMC-1
1	13.16 (18.93)	12.47 (15.62)
2	17.29 (25.90)	9.38 (11.79)
3	17.67 (26.70)	18.43 (26.30)
4	15.61 (22.01)	15.02 (16.86)
5	23.65 (31.74)	16.10 (20.36)
6	18.72 (27.52)	14.45 (16.61)
7	28.81 (37.23)	42.20 (48.10)

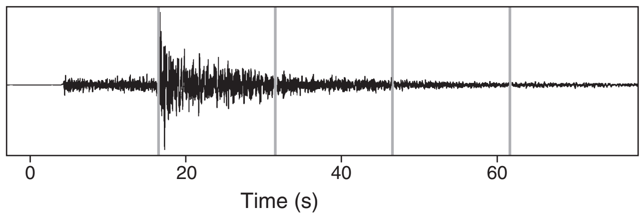

Fig. 3. An example of the seismogram used in this study. MLTWA processing was conducted by dividing three time windows (grey vertical line) with a length of 15 s starting from S-wave onset.

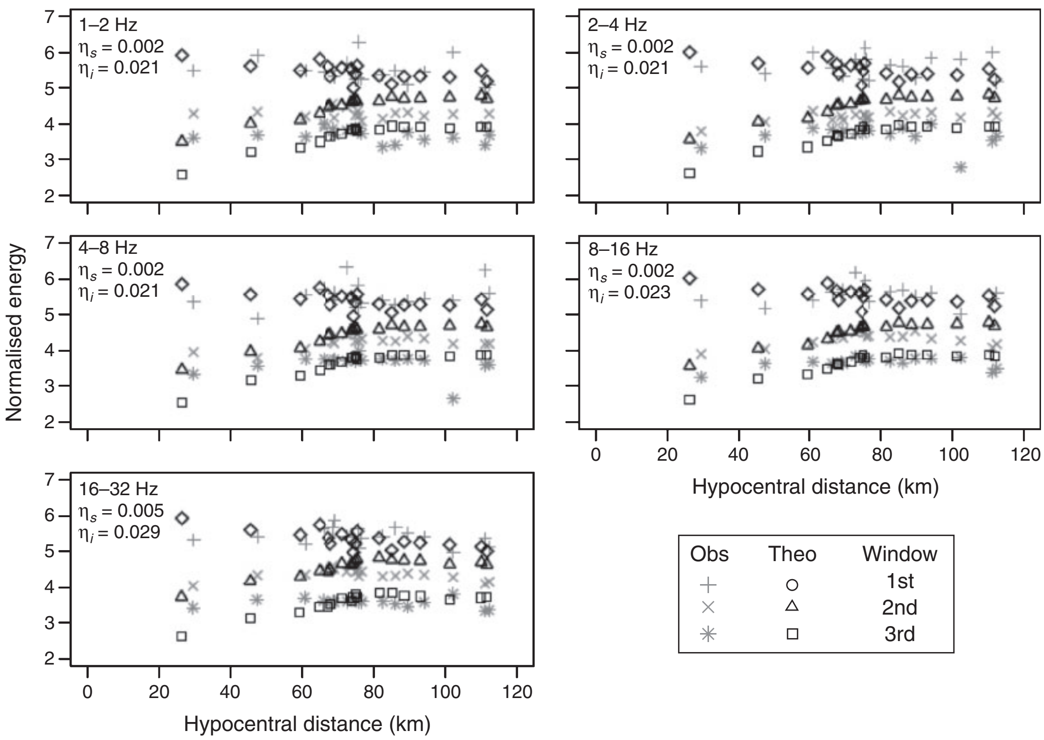

Fig. 4. For event 7, observed energy values (grey symbols) and theoretical energy values (black symbols) are compared for three windows at the least M_{sum} for five frequency-bands.

Table 3. Range of MLTWA parameters and Q^{-1} values for K-10 (Chung and Asep, 2013) and events 1, 3, 4, and 7, obtained by DSMC-1. Numbers in parentheses under the event number denote the number of record stations for the event.

Event no.	Freq. (Hz)	η_i (km^{-1})		η_s (km^{-1})		L_e^{-1} (km^{-1})		B_o		Q_i^{-1} ($\times 10^{-3}$)		Q_s^{-1} ($\times 10^{-3}$)		Q_t^{-1} ($\times 10^{-3}$)	
	1 – 2	0.020	+0.009 / –0.007	0.011	+0.015 / –0.005	0.031	+0.024 / –0.012	0.35	+0.76 / –0.10	7.43	+3.34 / –2.60	4.08	+5.57 / –1.86	11.51	+8.91 / –4.46
	2 – 4	0.017	+0.008 / –0.008	0.008	+0.009 / –0.004	0.025	+0.017 / –0.012	0.32	+0.47 / –0.11	3.16	+1.49 / –1.49	1.49	+1.67 / –0.74	4.64	+3.16 / –2.23
K-10 (41)	4 – 8	0.018	+0.008 / –0.007	0.008	+0.012 / –0.003	0.026	+0.020 / –0.010	0.31	+0.78 / –0.06	1.67	+0.74 / –0.65	0.74	+1.11 / –0.28	2.41	+1.86 / –0.93
	8 – 16	0.023	+0.008 / –0.008	0.014	+0.013 / –0.007	0.037	+0.021 / –0.015	0.38	+0.38 / –0.12	1.07	+0.37 / –0.37	0.65	+0.60 / –0.32	1.72	+0.97 / –0.70
	16 – 32	0.029	+0.008 / –0.007	0.021	+0.018 / –0.009	0.050	+0.026 / –0.016	0.42	+0.36 / –0.10	0.67	+0.19 / –0.16	0.49	+0.42 / –0.21	1.16	+0.60 / –0.37
	1 – 2	0.020	+0.011 / –0.005	0.007	+0.007 / –0.002	0.027	+0.018 / –0.007	0.26	+0.31 / –0.03	7.43	+4.08 / –1.86	2.60	+2.60 / –0.74	10.03	+6.68 / –2.60
	2 – 4	0.024	+0.009 / –0.012	0.012	+0.008 / –0.008	0.036	+0.017 / –0.020	0.33	+0.18 / –0.19	4.46	+1.67 / –2.23	2.23	+1.49 / –1.49	6.68	+3.16 / –3.71
1 (12)	4 – 8	0.025	+0.009 / –0.010	0.012	+0.009 / –0.006	0.037	+0.018 / –0.016	0.32	+0.22 / –0.11	2.32	+0.84 / –0.93	1.11	+0.84 / –0.56	3.44	+1.67 / –1.49
	8 – 16	0.029	+0.011 / –0.010	0.016	+0.016 / –0.007	0.045	+0.027 / –0.017	0.36	+0.41 / –0.09	1.35	+0.51 / –0.46	0.74	+0.74 / –0.32	2.09	+1.25 / –0.79
	16 – 32	0.042	+0.010 / –0.016	0.032	+0.012 / –0.012	0.074	+0.022 / –0.028	0.43	+0.08 / –0.09	0.97	+0.23 / –0.37	0.74	+0.28 / –0.28	1.72	+0.51 / –0.65
	1 – 2	0.024	+0.010 / –0.011	0.009	+0.012 / –0.005	0.033	+0.022 / –0.016	0.27	+0.54 / –0.11	8.91	+3.71 / –4.08	3.34	+4.46 / –1.86	12.25	+8.17 / –5.94
	2 – 4	0.022	+0.013 / –0.011	0.007	+0.013 / –0.004	0.029	+0.026 / –0.015	0.24	+0.92 / –0.11	4.08	+2.41 / –2.04	1.30	+2.41 / –0.74	5.38	+4.83 / –2.79
3 (13)	4 – 8	0.017	+0.012 / –0.007	0.004	+0.008 / –0.001	0.021	+0.020 / –0.008	0.19	+0.84 / –0.02	1.58	+1.11 / –0.65	0.37	+0.74 / –0.09	1.95	+1.86 / –0.74
	8 – 16	0.026	+0.012 / –0.010	0.017	+0.020 / –0.008	0.043	+0.032 / –0.018	0.40	+0.65 / –0.12	1.21	+0.56 / –0.46	0.79	+0.93 / –0.37	2.00	+1.49 / –0.84
	16 – 32	0.039	+0.011 / –0.014	0.042	+0.025 / –0.025	0.081	+0.036 / –0.039	0.52	+0.23 / –0.24	0.91	+0.26 / –0.32	0.97	+0.58 / –0.58	1.88	+0.84 / –0.91
	1 – 2	0.019	+0.006 / –0.013	0.007	+0.004 / –0.005	0.026	+0.010 / –0.018	0.27	+0.11 / –0.19	7.06	+2.23 / –4.83	2.60	+1.49 / –1.86	9.66	+3.71 / –6.68
	2 – 4	0.017	+0.005 / –0.010	0.007	+0.003 / –0.004	0.024	+0.008 / –0.014	0.29	+0.07 / –0.10	3.16	+0.93 / –1.86	1.30	+0.56 / –0.74	4.46	+1.49 / –2.60
4 (13)	4 – 8	0.018	+0.010 / –0.006	0.007	+0.010 / –0.003	0.025	+0.020 / –0.009	0.28	+0.65 / –0.07	1.67	+0.93 / –0.56	0.65	+0.93 / –0.28	2.32	+1.86 / –0.84
	8 – 16	0.022	+0.008 / –0.007	0.011	+0.012 / –0.004	0.033	+0.020 / –0.011	0.33	+0.45 / –0.06	1.02	+0.37 / –0.32	0.51	+0.56 / –0.19	1.53	+0.93 / –0.51
	16 – 32	0.027	+0.010 / –0.007	0.017	+0.019 / –0.006	0.044	+0.029 / –0.013	0.39	+0.56 / –0.06	0.63	+0.23 / –0.16	0.39	+0.44 / –0.14	1.02	+0.67 / –0.30
	1 – 2	0.026	+0.013 / –0.014	0.011	+0.026 / –0.008	0.037	+0.039 / –0.022	0.30	+1.82 / –0.20	9.66	+4.83 / –5.20	4.08	+9.66 / –2.97	13.74	+14.48 / –8.17
	2 – 4	0.017	+0.013 / –0.007	0.004	+0.010 / –0.001	0.021	+0.023 / –0.008	0.19	+1.30 / –0.22	3.16	+2.41 / –1.30	0.74	+1.86 / –0.19	3.90	+4.27 / –1.49
7 (18)	4 – 8	0.019	+0.015 / –0.009	0.006	+0.018 / –0.003	0.025	+0.033 / –0.012	0.24	+2.36 / –0.08	1.76	+1.39 / –0.84	0.56	+1.67 / –0.28	2.32	+3.06 / –1.11
	8 – 16	0.026	+0.010 / –0.009	0.011	+0.013 / –0.007	0.037	+0.023 / –0.016	0.30	+0.47 / –0.15	1.21	+0.46 / –0.42	0.51	+0.60 / –0.32	1.72	+1.07 / –0.74
	16 – 32	0.034	+0.007 / –0.011	0.024	+0.021 / –0.011	0.058	+0.028 / –0.022	0.41	+0.36 / –0.11	0.79	+0.16 / –0.26	0.56	+0.49 / –0.26	1.35	+0.65 / –0.51

Table 4. Range of MLTWA parameters and Q^{-1} values for K-10 (Chung and Asep, 2013) and events 1, 3, 4, and 7, obtained by DSMC-2. Numbers in parentheses under the event number denote the number of record stations for the event.

Event no.	Freq. (Hz)	η_i (km^{-1})		η_s (km^{-1})		L_e^{-1} (km^{-1})		B_o		Q_i^{-1} ($\times 10^{-3}$)		Q_s^{-1} ($\times 10^{-3}$)		Q_t^{-1} ($\times 10^{-3}$)	
	1 – 2	0.022	+ 0.008	0.003	+ 0.006	0.025	+ 0.014	0.12	+ 0.50	8.17	+ 2.97	1.11	+ 2.23	9.28	+ 5.20
			– 0.004		– 0.001		– 0.005		– 0.02		– 1.49		– 0.37		– 1.86
	2 – 4	0.021	+ 0.010	0.003	+ 0.007	0.024	+ 0.017	0.13	+ 0.71	3.90	+ 1.86	0.56	+ 1.30	4.46	+ 3.16
			– 0.004		– 0.001		– 0.005		– 0.11		– 0.74		– 0.19		– 0.93
1	4 – 8	0.022	+ 0.012	0.003	+ 0.009	0.025	+ 0.021	0.12	+ 1.12	2.04	+ 1.11	0.28	+ 0.84	2.32	+ 1.95
(12)			– 0.003		– 0.001		– 0.004		– 0.01		– 0.28		– 0.09		– 0.37
	8 – 16	0.030	+ 0.007	0.008	+ 0.007	0.038	+ 0.014	0.21	+ 0.17	1.39	+ 0.32	0.37	+ 0.32	1.76	+ 0.65
			– 0.008		– 0.005		– 0.013		– 0.09		– 0.37		– 0.23		– 0.60
	16 – 32	0.036	+ 0.004	0.010	+ 0.005	0.046	+ 0.009	0.22	+ 0.06	0.84	+ 0.09	0.23	+ 0.12	1.07	+ 0.21
			– 0.004		– 0.003		– 0.007		– 0.02		– 0.09		– 0.07		– 0.16
	1 – 2	0.023	+ 0.006	0.003	+ 0.001	0.026	+ 0.007	0.12	+ 0.02	8.54	+ 2.23	1.11	+ 0.37	9.66	+ 2.60
			– 0.004		– 0.001		– 0.005		– 0.01		– 1.49		– 0.37		– 1.86
	2 – 4	0.023	+ 0.005	0.003	+ 0.003	0.026	+ 0.008	0.12	+ 0.12	4.27	+ 0.93	0.56	+ 0.56	4.83	+ 1.49
			– 0.004		– 0.001		– 0.005		– 0.01		– 0.74		– 0.19		– 0.93
3	4 – 8	0.022	+ 0.004	0.003	+ 0.001	0.025	+ 0.005	0.12	+ 0.02	2.04	+ 0.37	0.28	+ 0.09	2.32	+ 0.46
(13)			– 0.008		– 0.002		– 0.010		– 0.06		– 0.74		– 0.19		– 0.93
	8 – 16	0.023	+ 0.010	0.004	+ 0.010	0.027	+ 0.020	0.15	+ 0.97	1.07	+ 0.46	0.19	+ 0.46	1.25	+ 0.93
			– 0.006		– 0.002		– 0.008		– 0.04		– 0.28		– 0.09		– 0.37
	16 – 32	0.032	+ 0.008	0.011	+ 0.014	0.043	+ 0.022	0.26	+ 0.45	0.74	+ 0.19	0.26	+ 0.32	1.00	+ 0.51
			– 0.006		– 0.004		– 0.010		– 0.04		– 0.14		– 0.09		– 0.23
	1 – 2	0.018	+ 0.005	0.002	+ 0.001	0.020	+ 0.006	0.10	+ 0.03	6.68	+ 1.86	0.74	+ 0.37	7.43	+ 2.23
			– 0.003		– 0.000		– 0.003		– 0.00		– 1.11		– 0.00		– 1.11
	2 – 4	0.015	+ 0.006	0.002	+ 0.002	0.017	+ 0.008	0.12	+ 0.13	2.79	+ 1.11	0.37	+ 0.37	3.16	+ 1.49
			– 0.006		– 0.001		– 0.007		– 0.08		– 1.11		– 0.19		– 1.30
4	4 – 8	0.015	+ 0.007	0.003	+ 0.004	0.018	+ 0.011	0.17	+ 0.33	1.39	+ 0.65	0.28	+ 0.37	1.67	+ 1.02
(13)			– 0.006		– 0.000		– 0.006		– 0.00		– 0.56		– 0.00		– 0.56
	8 – 16	0.017	+ 0.016	0.002	+ 0.005	0.019	+ 0.021	0.11	+ 0.72	0.79	+ 0.74	0.09	+ 0.23	0.88	+ 0.97
			– 0.003		– 0.000		– 0.003		– 0.00		– 0.14		– 0.00		– 0.14
	16 – 32	0.020	+ 0.003	0.002	+ 0.011	0.022	+ 0.014	0.09	+ 2.77	0.46	+ 0.07	0.05	+ 0.26	0.51	+ 0.32
			– 0.013		– 0.000		– 0.013		– 0.00		– 0.30		– 0.00		– 0.30
	1 – 2	0.021	+ 0.004	0.002	+ 0.006	0.023	+ 0.010	0.09	+ 0.79	7.80	+ 1.49	0.74	+ 2.23	8.54	+ 3.71
			– 0.003		– 0.001		– 0.004		– 0.02		– 1.11		– 0.37		– 1.49
	2 – 4	0.021	+ 0.005	0.002	+ 0.007	0.023	+ 0.012	0.09	+ 1.08	3.90	+ 0.93	0.37	+ 1.30	4.27	+ 2.23
			– 0.006		– 0.001		– 0.007		– 0.18		– 1.11		– 0.19		– 1.30
7	4 – 8	0.021	+ 0.004	0.002	+ 0.009	0.023	+ 0.013	0.09	+ 1.77	1.95	+ 0.37	0.19	+ 0.84	2.14	+ 1.21
(18)			– 0.003		– 0.001		– 0.004		– 0.02		– 0.28		– 0.09		– 0.37
	8 – 16	0.023	+ 0.003	0.002	+ 0.007	0.025	+ 0.010	0.08	+ 0.99	1.07	+ 0.14	0.09	+ 0.32	1.16	+ 0.46
			– 0.003		– 0.005		– 0.008		– 0.50		– 0.14		– 0.23		– 0.37
	16 – 32	0.029	+ 0.007	0.005	+ 0.005	0.034	+ 0.012	0.15	+ 0.16	0.67	+ 0.16	0.12	+ 0.12	0.79	+ 0.28
			– 0.008		– 0.003		– 0.011		– 0.06		– 0.19		– 0.07		– 0.26

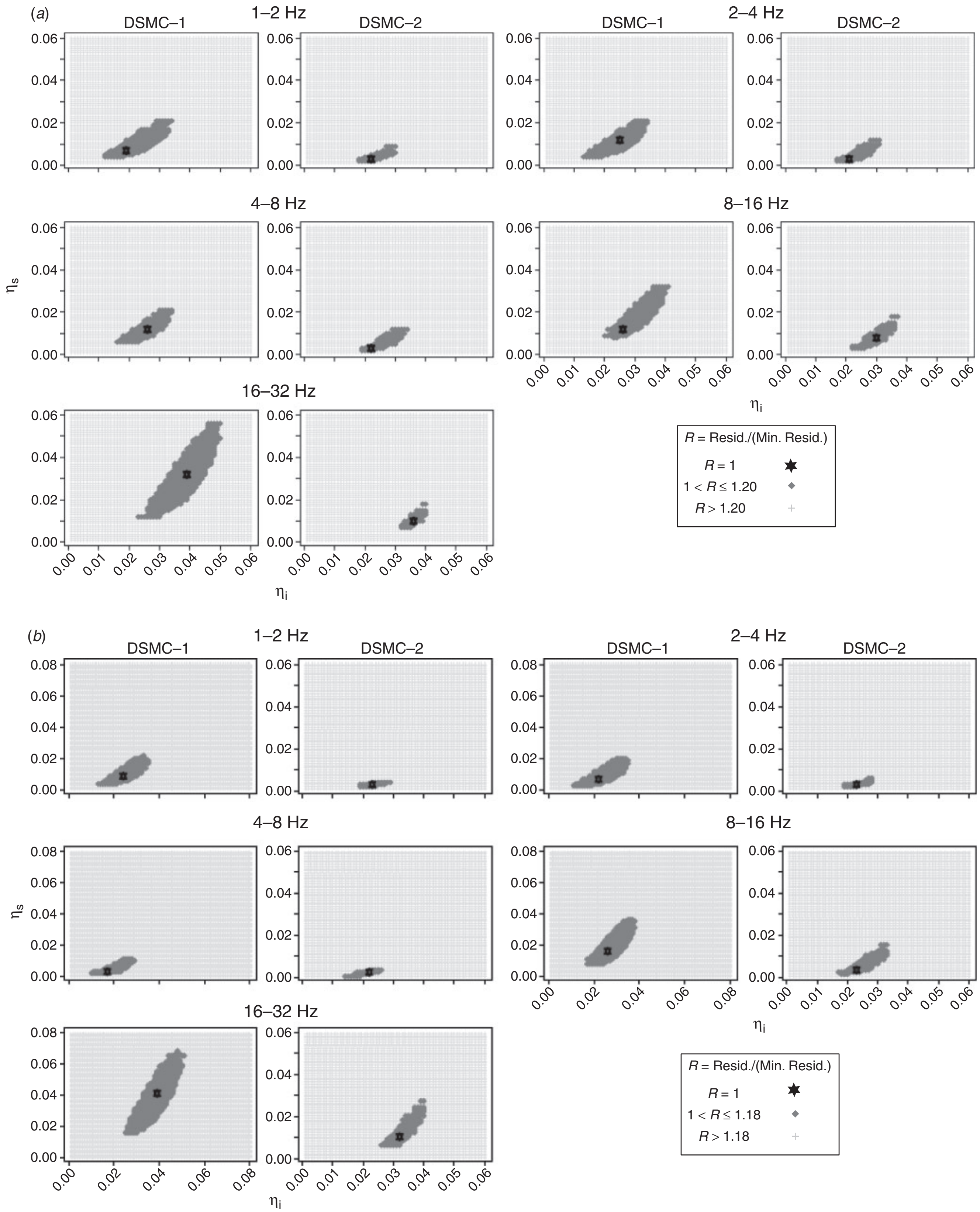

Fig. 5. Comparison of residual map of four events between DSMC-1 and DSMC-2, which were normalised to its minimum (✱) for five frequency-bands. The shaded areas represent a confidence zone of the *F* test at the 60% level. (*a*) Event 1, (*b*) event 4, (*c*) event 5, and (*d*) event 7.

processing step was removing the trend and the mean values and the application of a 5% cosine taper to each end of the time series of a seismogram. Then, the seismogram was filtered by a four-pole Butterworth band-pass filter centred at five frequencies: 1.5 Hz, 3 Hz, 6 Hz, 12 Hz, and 24 Hz. The filtering used a low-pass Gaussian Nadaraya–Watson kernel regression smoother (R Development Core Team, 2006). After estimating the noise during the 5 s before the P-waves arrival, further processing was done for only seismograms with a signal/noise ratio greater than 2.

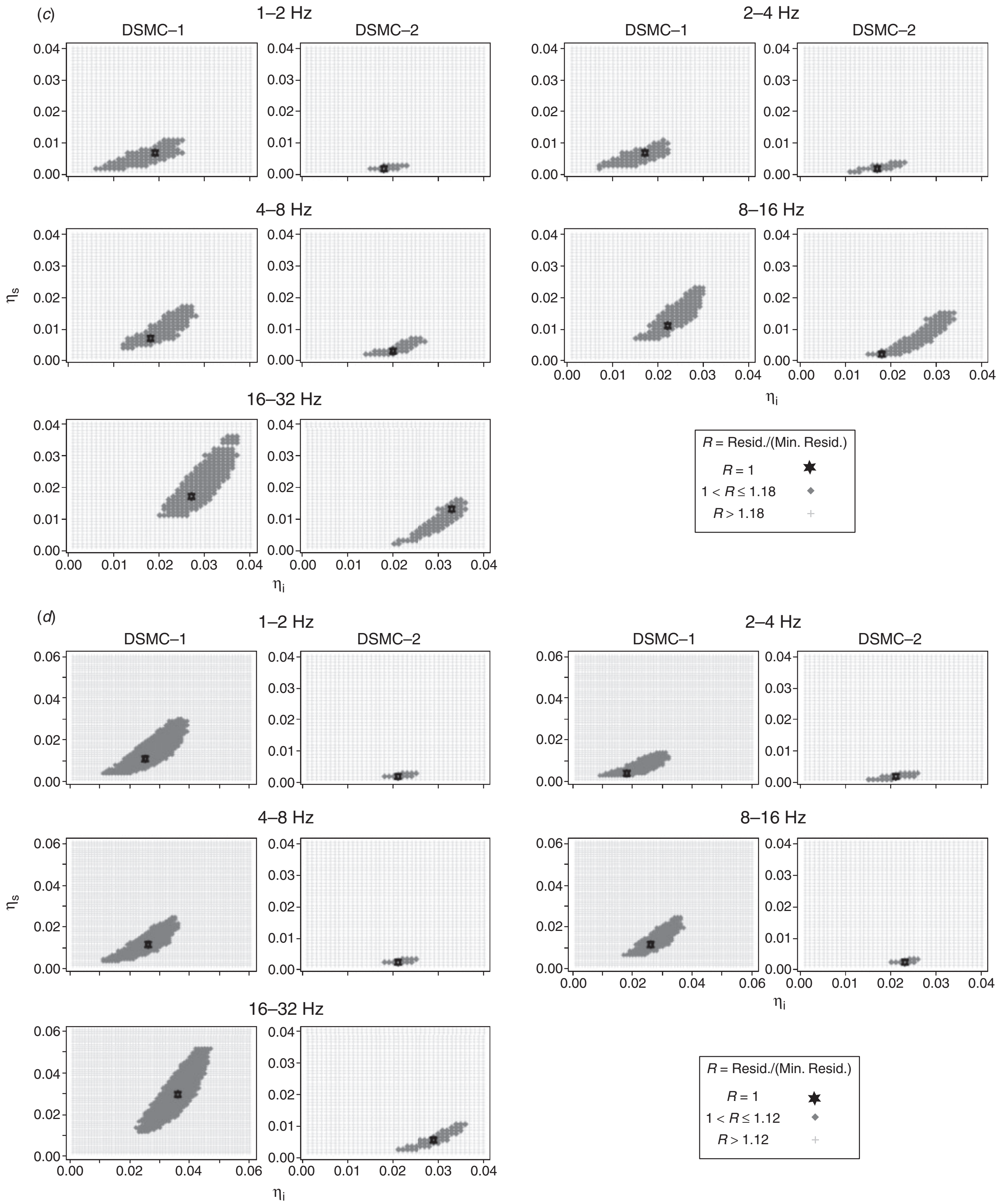

Fig. 5. *(continued)*

From the three windows (Figure 3) for the processed seismograms, the seismic energies were obtained by integrating the squared amplitudes over time for the seismograms. The geometrical spreading effect was corrected by multiplication of $4\pi r^2$, where r is the hypocentral distance. In addition, each integral was normalised by the coda spectral amplitude of a 10 s time window centred at 45 s to correct different sources and site effects (Hoshiba, 1993). Whereas the observed values of the envelope energy were obtained by the aforementioned procedure, the theoretical values were derived from the methods of DSMC-1 and 2 for the uniform velocity (= 3.5 km/s) model. For least-square estimates of the attenuation coefficients of intrinsic (η_i) and scattering (η_s), a grid-search with an interval of 0.001 km^{-1} was done to find the minimum values of the misfit function M_f for each frequency f (Hoshiba, 1991):

$$M_f(\eta_s, \eta_i) = \sum_{k=1}^{N} \sum_{j=1}^{3} (EO_j(r_k) - EM_j(r_k))^2, \tag{6}$$

where k and j are the number of observations and time windows, respectively. EO_j (r_k) and EM_j (r_k) present the observed and theoretical energies, respectively. Comparisons of theoretical with observed values are exemplified in Figure 4. The sum of the misfit function, M_{sum}, is given by combining the misfit function for each frequency:

$$M_{sum}(\eta_i, \eta_s) = \sum_{f=1}^{5} M_f(\eta_i, \eta_s). \tag{7}$$

Because the radiation pattern is naturally a large influence near the source range, we empirically find weight factors for the residuals between observed and theoretical values, twice for distances less than 80 km. Through this distance-weighting, M_{sum} of DSMC-2 is decreased more than that of DSMC-1 (Table 2). The error intervals of the two attenuation coefficients for each frequency (Tables 3 and 4) were evaluated from the confidence contour using the F distribution test (Draper and Smith, 1998) as follows:

$$M_f(\eta_s, \eta_i) = M_f(\hat{\eta}_s, \hat{\eta}_i)\left[1 + \frac{p}{n-p} F_{60}(p, n-p)\right], \tag{8}$$

where $M_f(\hat{\eta}_s, \hat{\eta}_i)$ is the minimum value of $M_f(\eta_s, \eta_i)$, the number of model parameter is p = 2(η_s and η_i) and n is the number of observations. F_{60} denotes the Fisher distribution function with a confidence level of 60%, which was also used by previous studies (Bianco et al., 2002, 2005; Giampiccolo et al., 2006). The ratios $M_f(\eta_s, \eta_i)/M_f(\hat{\eta}_s, \hat{\eta}_i)$ were depicted by the shading zones for the confidence areas (Figure 5). The seismic albedo, $B_0 = \eta_s/(\eta_i + \eta_s)$, and the inverse of the extinction length, $L_e^{-1} = \eta_i + \eta_s$, are also shown in Tables 3 and 4. The seismic albedo represents a dimensionless ratio of scattering loss to total attenuation, whereas, the inverse of the extinction length describes the inverse of the distance over which the primary S-wave energy is decreased by exponent (e).

Results and discussion

Through application of distance weighting, DSMC-2 shows smaller M_{sum} than that of DSMC-1 for events 3 and 7, and similar M_{sum} for events 1 and 4 (Table 2). The focal mechanisms of events showing smaller or similar M_{sum} were considered as reliable, and only events 1, 3, 4 and 7 are exemplified in Figures 4 and 5 and Tables 3 and 4. In particular, event 7 shows significantly smaller M_{sum} of DSMC-

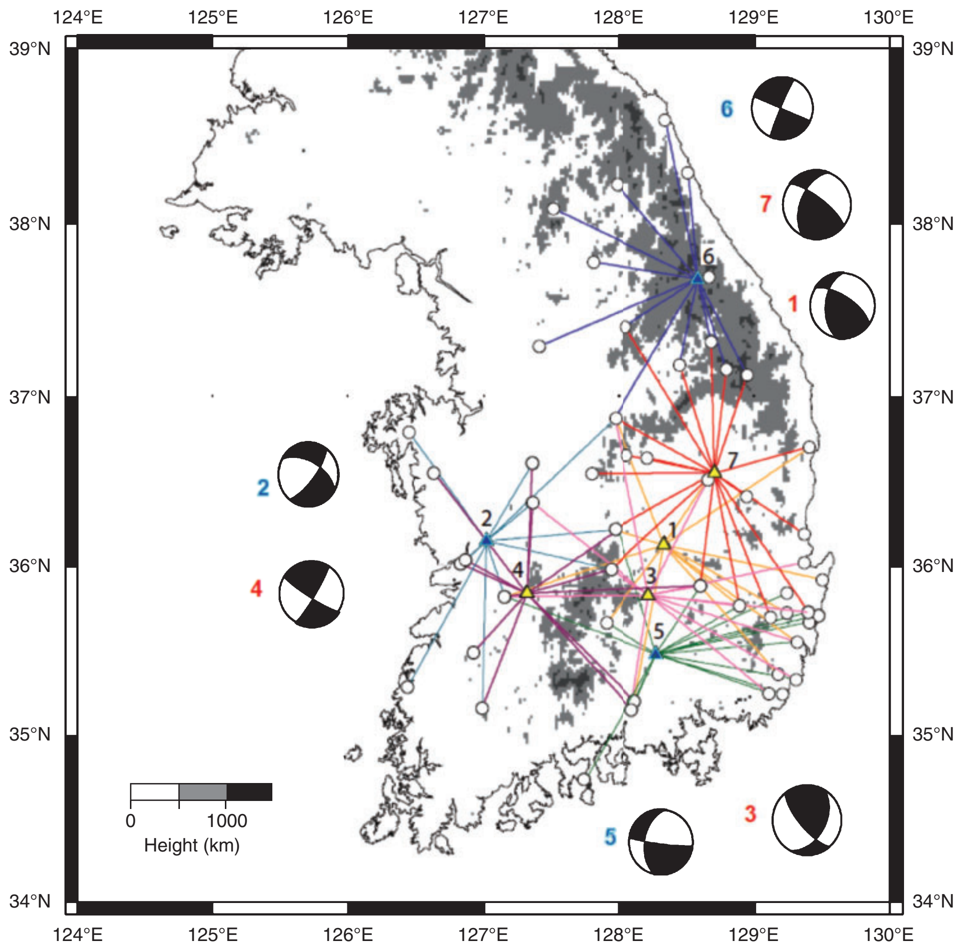

Fig. 6. Topographic maps of the events (triangles) with their focal mechanism solutions in Table 1 and recorded stations (circles). Events 1, 3, 4 and 7, which showed reliable results for DSMC-2, are denoted by yellow triangles connected by lines of colour (yellow, pink, purple and red, respectively), and with red numbers for focal mechanism. The other events 2, 5 and 6 are denoted by blue triangles connected by light blue, green and dark blue lines, respectively, and by blue numbers for focal mechanism.

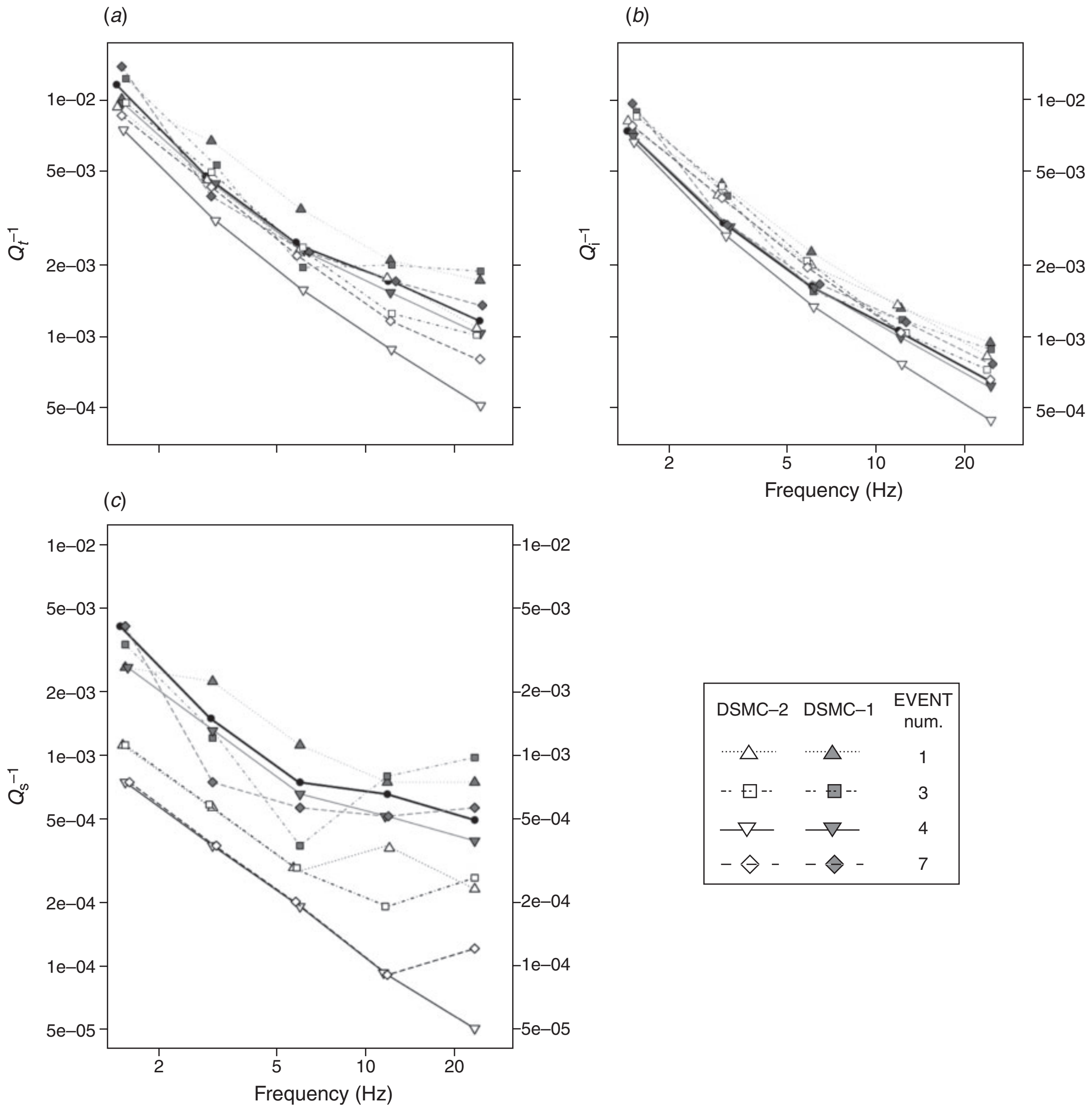

Fig. 7. Comparison of Q^{-1} values for K-10 (Chung and Asep, 2013) and events 1, 3, 4 and 7 obtained by DSMC-1 and DSMC-2. (*a*) $1/Q_t$, (*b*) $1/Q_i$, and (*c*) $1/Q_s$.

2 than that of DSMC-1, even without the application of distance weighting. This reliability of event 7 seems to be related to the best azimuthal coverage among the data events (Figure 6). Although event 6 is the largest event, and the focal mechanism is well defined, the M_{sum} of DSMC-2 is larger than that of DMSC-1. This might be related to the topographic effect, whose contribution of amplitude variation is well known in rough terrain (Geli et al., 1988; Rodgers et al., 2010). The location of event 6 shows rough topography with a high mountainous area (Figure 6), which possibly caused amplitude errors in the waveform inversion using the simplified one-dimensional model.

Despite using the focal mechanism, however, improvements of M_{sum} were not significant for many events. This is thought to be due to the uncertainty of the focal mechanism, which is generally known to be large for small and shallow earthquakes, as in our data (Helffrich, 1997). The small magnitude of event 5 is attributed to larger M_{sum} of DSMC-2 than that of DSMC-1, in spite of the second-most numerous recorded stations. In Figure 7, the Q_s^{-1} values for DSMC-2 are low compared with those for DSMC-1 and Chung and Asep's (2013) results, which were also performed by DSMC-1. However, the Q_s^{-1} values are consistent with the Q_s^{-1} values obtained by Lee et al. (2010) in Kyeongsang Basin. The low Q_s^{-1} values would imply that the intrinsic absorption predominates in our study region.

The DSMC-2 method requires more computations than the DSMC-1 method to complement the small size of receivers. We increased the total number of particles and decreased the interval of time steps in the DSMC-2 process. These parameters should be determined to stabilise the number of arrived particles and retain temporal resolution.

Acknowledgements

This research was supported by funds from CATER 2012–8010 provided by the Center for Atmosphere Sciences and Earthquake Research (CATER) of Korea.

References

Aki, K., and Richards, P., 1980, *Quantitative seismology*: W. H. Freeman.

Asep, N. R., Chung, T. W., and Yoshimoto, K., 2014, Separation of intrinsic and scattering attenuation using single event source in South Korea: *Bulletin of the Seismological Society of America*, in press.

Bianco, F., Del Pezzo, E., Castellano, M., Ibanez, J., and Di Luccio, F., 2002, Separation of intrinsic and scattering seismic attenuation in the Southern Apennine zone, Italy: *Geophysical Journal International*, **150**, 10–22. doi:10.1046/j.1365-246X.2002.01696.x

Bianco, F., Del Pezzo, E., Malagnini, L., Di Luccio, F., and Akinci, A., 2005, Separation of depth-dependent intrinsic and scattering seismic attenuation in the northeastern sector of the Italian Peninsula: *Geophysical Journal International*, **161**, 130–142. doi:10.1111/j.1365-246X.2005.02555.x

Cervený, V., and Ravindra, R., 1971, *Theory of seismic head waves*: University of Toronto Press.

Chung, T. W., 2014, Quantitative study of the separation of intrinsic and scattering seismic attenuation in southeastern Korea using the Monte Carlo simulation method: *Disaster Advances*, **7**, 7–17.

Chung, T. W., and Asep, N. R., 2013, Multiple lapse time window analysis of the Korean Peninsula considering focal depth: *Journal of the Korean Society of Earth and Exploration Geophysicists*, **16**, 293–299. [in Korean]

Chung, T. W., Yoshimoto, K., and Yun, S., 2010, The separation of intrinsic and scattering seismic attenuation in South Korea: *Bulletin of the Seismological Society of America*, **100**, 3183–3193. doi:10.1785/0120100054

Dainty, A. M., 1981, A scattering model to explain seismic Q observation in the lithosphere between 1 and 30 Hz: *Geophysical Research Letters*, **8**, 1126–1128. doi:10.1029/GL008i011p01126

Draper, N. R., and Smith, H., 1998, *Applied regression analysis*: John Wiley.

Fehler, M. C., Hoshiba, M., and Sato, H., 1992, Separation of scattering and intrinsic attenuation for the Kanto-Tokai region, Japan, using measurements of S-wave energy versus hypocentral distance: *Geophysical Journal International*, **108**, 787–800. doi:10.1111/j.1365-246X.1992.tb03470.x

Feynman, R. P., Leighton, R. B., and Sands, M., 1989, *The Feynman lectures on physics, volume 1*: Addison-Wesley.

Geli, L., Bard, P.-Y., and Jullen, B., 1988, The effect of topography on earthquake ground motion: a review and new results: *Bulletin of the Seismological Society of America*, **78**, 42–63.

Giampiccolo, E., Tuvé, T., Gresta, S., and Patané, D., 2006, S-waves attenuation and separation of scattering and intrinsic absorption of seismic energy in southeastern Sicily (Italy): *Geophysical Journal International*, **165**, 211–222. doi:10.1111/j.1365-246X.2006.02881.x

Helffrich, G. R., 1997, How good are routinely determined focal mechanism? Empirical statistics based on a comparison of Harvard, USGS, and ERI moment tensors: *Geophysical Journal International*, **131**, 741–750. doi:10.1111/j.1365-246X.1997.tb06609.x

Hong, T.-K., and Choi, H., 2012, Seismological constraints on the collision belt between the North and South China blocks in the Yellow Sea: *Tectonophysics*, **570–571**, 102–113. doi:10.1016/j.tecto.2012.08.034

Hoshiba, M., 1991, Simulation of multiple-scattered coda wave excitation based on the energy conservation law: *Physics of the Earth and Planetary Interiors*, **67**, 123–136. doi:10.1016/0031-9201(91)90066-Q

Hoshiba, M., 1993, Separation of scattering attenuation and intrinsic absorption in Japan using the multiple lapse time window analysis of full seismogram envelope: *Journal of Geophysical Research*, **98**, 15 809–15 824. doi:10.1029/93JB00347

Hoshiba, M., 1997, Seismic coda wave envelope in depth-dependent S wave velocity structure: *Physics of the Earth and Planetary Interiors*, **104**, 15–22. doi:10.1016/S0031-9201(97)00055-1

Hoshiba, M., Sato, H., and Fehler, M. C., 1991, Numerical basis of the separation of scattering and intrinsic absorption from full seismogram envelope: a Monte Carlo simulation of multiple isotropic scaterring: *Papers in Meteorology and Geophysics*, **42**, 65–91. doi:10.2467/mripapers.42.65

Lee, W. S., Yun, S., and Do, J.-Y., 2010, Scattering and intrinsic attenuation of short-period *S* waves in the Gyeongsang Basin, South Korea, revealed from *S*-wave seismogram envelopes based on the radiative transfer theory: *Bulletin of the Seismological Society of America*, **100**, 833–840. doi:10.1785/0120090149

Mitchell, B. J., 1995, Anelastic structure and evolution of the continental crust and upper mantle from seismic wave attenuation: *Reviews of Geophysics*, **33**, 441–462. doi:10.1029/95RG02074

Mitchell, B. J., and Xie, J., 1994, Attenuation of multiphase surface waves in the Basin and Range Province – III. Inversion for crustal anelasticity: *Geophysical Journal International*, **116**, 468–484. doi:10.1111/j.1365-246X.1994.tb01809.x

Park, J.-C., Kim, W., Chung, T. W., Baag, C.-E., and Ree, J.-H., 2007, Focal mechanisms of recent earthquakes in the Southern Korean Peninsula: *Geophysical Journal International*, **169**, 1103–1114. doi:10.1111/j.1365-246X.2007.03321.x

R Development Core Team, 2006, *R: A language and environment for statistical computing, reference index version 2.2.1*: R Foundation for Statistical Computing. Available at http://www.R-project.org

Rodgers, A. J., Petersson, N. A., and Sjogreen, B., 2010, Simulation of topographic effects on seismic waves from shallow explosions near the North Korean nuclear test site with emphasis on shear wave generation: *Journal of Geophysical Research*, **115**, B11309. doi:10.1029/2010JB007707

Sato, H., 1993, Energy transportation in one- and two-dimensional scattering media: analytic solutions of the multiple isotropic scattering model: *Geophysical Journal International*, **112**, 141–146. doi:10.1111/j.1365-246X.1993.tb01443.x

Sato, H., Fehler, M. C., and Maeda, T., 2012, *Seismic wave propagation and scattering in the heterogeneous earth* (2nd edition): Springer-Verlag, Inc.

Yoshimoto, K., 2000, Monte Carlo simulation of seismogram envelopes in scattering media: *Journal of Geophysical Research*, **105**, 6153–6161. doi:10.1029/1999JB900437

Yoshimoto, K., Sato, H., and Ohtake, M., 1993, Frequency-dependent attenuation of *P* and *S*-waves in the Kanto area, Japan, based on the coda-normalization method: *Geophysical Journal International*, **114**, 165–174. doi:10.1111/j.1365-246X.1993.tb01476.x

Zeng, Y., Su, F., and Aki, K., 1991, Scattering wave energy propagation in a random isotropic scattering medium: 1, Theory: *Journal of Geophysical Research*, **96**, 607–619. doi:10.1029/90JB02012